Oscillatory states in thermal convection of a paramagnetic fluid in a cubical enclosure subjected to a magnetic field gradient

S. Kenjereš

Faculty of Applied Sciences and J. M. Burgerscentre for Fluid Dynamics, Delft University of Technology, Leeghwaterstraat 39, 2628 CB Delft, The Netherlands

L. Pyrda, W. Wrobel, E. Fornalik-Wajs, and J. S. Szmyd

Department of Fundamental Research in Energy Engineering, Faculty of Energy and Fuels, AGH University of Science and Technology 30 Mickiewicza Avenue, 30059 Krakow, Poland

(Received 14 October 2011; revised manuscript received 29 December 2011; published 20 April 2012)

We report experimental and numerical studies of combined natural and magnetic convection of a paramagnetic fluid inside a cubical enclosure heated from below and cooled from above and subjected to a magnetic field gradient. Values of the magnetic field gradient are in the range $9 \leqslant |\mathrm{grad}|b_0|^2| \leqslant 900\ \mathrm{T}^2/\mathrm{m}$ for imposed magnetic field strengths in the center of the superconducting magnet bore of $1 \leqslant |b_0|_{\max} \leqslant 10$ T. Very good agreement between experiments and simulation is obtained in predicting the integral heat transfer over the entire range of working parameters (i.e., thermal Rayleigh number $1.15 \times 10^5 \leqslant \mathrm{Ra_T} \leqslant 8 \times 10^6$, Prandtl number $5 \leqslant \mathrm{Pr} \leqslant 700$, and magnetization number $0 \leqslant \gamma \leqslant 58.5$). We present a stability diagram containing three characteristic states: steady, oscillatory (periodic), and turbulent regimes. The oscillatory states are identified for intermediate values of Pr ($40 \leqslant \mathrm{Pr} \leqslant 70$) and low magnetic field ($|b_0|_{\max} \leqslant 2$ T). Turbulent states are generated from initially stable flow and heat transfer regimes in the range of $70 \leqslant \mathrm{Pr} \leqslant 500$ for sufficiently strong magnetic field ($|b_0|_{\max} \geqslant 4$ T).

DOI: 10.1103/PhysRevE.85.046312 PACS number(s): 44.25.+f, 47.11.Df, 47.20.Bp, 47.65.Cb

Natural convection for heated-from-below configurations serves as a paradigm for a wide range of environmental, astrophysical, and industrial applications [1]. An interesting case of thermal convection is when the working fluid becomes magnetized in the presence of an external magnetic field. In such a case, in addition to gravity, the magnetization force is also important. By changing the strength and orientation of the imposed magnetic field, additional possibilities for affecting flow and heat transfer can be investigated. Possible areas of application where magnetic fields can be used to control flow and heat transfer include control of the growth rate and microstructure of materials [2] or protein crystals [3]. Starting from the pioneering work of Braithwaite *et al*. [4], the potential for magnetically controlled convection in paramagnetic, or even in ordinary (mainly diamagnetic), fluids (water) has been investigated both experimentally and numerically, e.g., [5–12]. A major contribution of these studies was in providing the integral heat transfer (Nusselt number) behavior under strong magnetic field gradients and in reporting some basic flow visualisations. All these studies addressed steady laminar flow regimes. The goal of our present investigation is to extend the range of working parameters toward transitional or potentially turbulent flow regimes. This is achieved, first, by employing significantly larger magnetic field gradients generated by state-of-the-art superconducting helium-free magnets (up to 900 T^2/m for magnetic field strength of 10 T, in contrast to up to 200 T^2/m for magnetic field strength of 5 T in previous studies); second, by using fluids with lower Prandtl numbers; and, finally, by performing a series of three-dimensional time-dependent simulations that revealed detailed insights into the dynamics and spatial reorganization of flow and thermal structures. Strong magnetic field gradients are generated by the superconducting helium-free magnet shown in Fig. 1. The calculated distributions of the magnetic field and resulting gradients for the upper limit of working conditions are shown in Fig. 2. The cubical enclosure can be positioned at different locations along the vertical axis of the superconducting magnet and combined effects (subtractive or additive) of the gravitational and magnetization forces can be generated. The suppression of the flow and heat transfer can be obtained by locating a cubical enclosure in the lower part of the bore, i.e., at $y = 0$, $z \leqslant 0$ m; see Fig. 2. In the present study, we focus our investigations on possible flow and heat transfer enhancements, i.e., situations where the generated magnetization force will support its gravitational counterpart. To achieve this, a cubical enclosure with dimensions $L = H = D = 0.032$ m is located in the upper part of the bore with its center at $y = 0$ and $z = 0.11$ m; Fig. 2. The experimental enclosure is constructed to provide an easy and controllable heating or cooling of the thermally active horizontal walls that are made from copper plates (Fig. 1, bottom). The sidewalls are made from plexiglass. The heating is done by nichrome wire placed just below the heated plate. The electric voltage and electric current for the nichrome wire are recorded by multimeters. The cooling is imposed by running water through a thermostating bath. The temperature of the copper plates is measured by T-type sheathed thermocouples inserted into plates. The integral heat transfer coefficient (Nusselt number) is calculated as the ratio between the net convective heat transfer rate and the net pure conduction contribution. More details of the experimental apparatus, the process of measuring the conductive and convective heat transfer, and the heat loss estimation are given in Ref. [12].

For experimental studies, three different paramagnetic fluids are analyzed: 80% (Pr = 584), 50% (Pr = 120), and 0% (Pr = 19) by volume aqueous solutions of glycerol with 0.8 mol/kg of solution concentration of gadolinium nitrate hexahydrate [$\mathrm{Gd(NO_3)_3{\cdot}6H_2O}$]. For example, the fluid

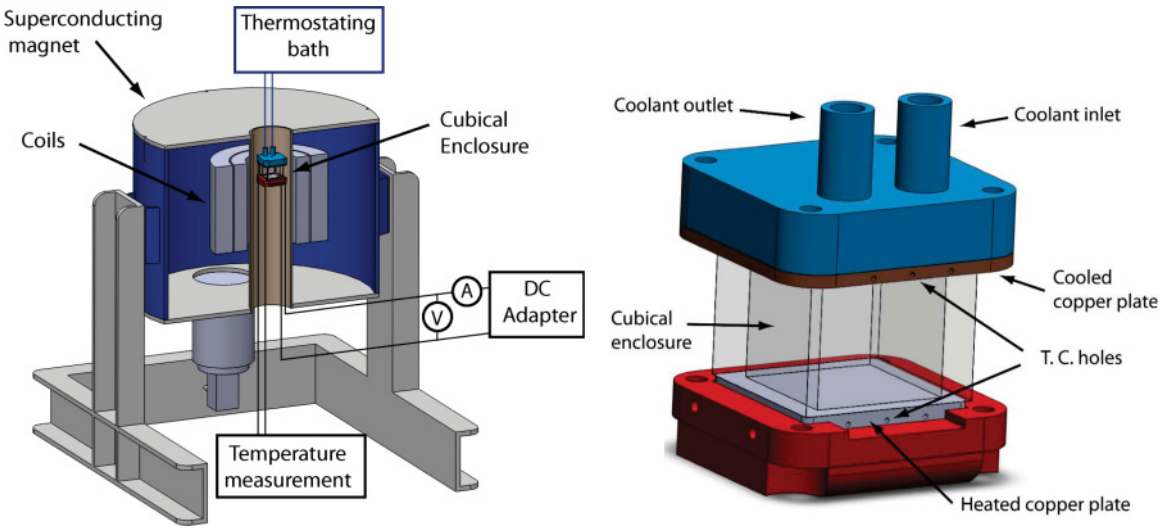

FIG. 1. (Color online) Left: Sketch of the experimental setup and location of the cubical enclosure with paramagnetic working fluid. The superconducting helium-free magnet (model HF10-100-VHT-B, Sumitomo Heavy Industries, Ltd., Japan) can generate up to 10 T in the magnet bore which has a diameter of 0.1 m and length of 0.5 m. Right: Cubical enclosure ($L = D = H = 0.032$ m) with copper plates and coolant inlet and outlet.

properties for Pr = 584 are $\rho = 1463$ kg/m^3, $\mu = 8.69 \times 10^{-2}$ Pa s, $\beta = 5.2 \times 10^{-4}$ K^{-1}, and $\chi = 2.31 \times 10^{-7}$. Before carrying out experiments, three-dimensional and time-dependent numerical simulations of flow and heat transfer are performed over a wide range of Pr ($5 \leqslant \mathrm{Pr} \leqslant 700$) and for different magnetic field intensities ($0 \leqslant |b_0|_{\max} \leqslant 12$ T) and their gradients. Our goal is to trace some potentially interesting oscillatory flow and heat transfer states. Note that throughout the paper we are defining the magnetic field strength condition to identify different flow regimes since it is a simple and easily controllable parameter in experimental investigations, although the magnetic field gradient is the main driving mechanism behind the magnetization force.

The system of equations describing the flow and heat transfer of a paramagnetic fluid subjected to a magnetic field consists of laws of conservation of mass, momentum, and energy. Note that for the paramagnetic fluids considered here, the total magnetic field is $\mathbf{b} = \mu_0(\mathbf{h} + \mathbf{m})$. Here, $\mathbf{h}$ is the external magnetic field, $\mathbf{m}(\mathbf{m} = \chi \cdot \mathbf{h})$ is the magnetization, χ is the magnetic susceptibility, and $\mu_0 = 4\pi \times 10^{-7}$ H/m is the magnetic constant. Since $\chi \ll 1$, it follows that $\mathbf{h} = \mathbf{b}/\mu_0$. The extended momentum equation is

$$\frac{\partial \mathbf{u}}{\partial t} + (\mathbf{u} \cdot \nabla)\mathbf{u} = -\frac{1}{\rho}\nabla p + \nu \nabla^2 \mathbf{u} + \mathbf{f}^B + \mathbf{f}^M, \qquad (1)$$

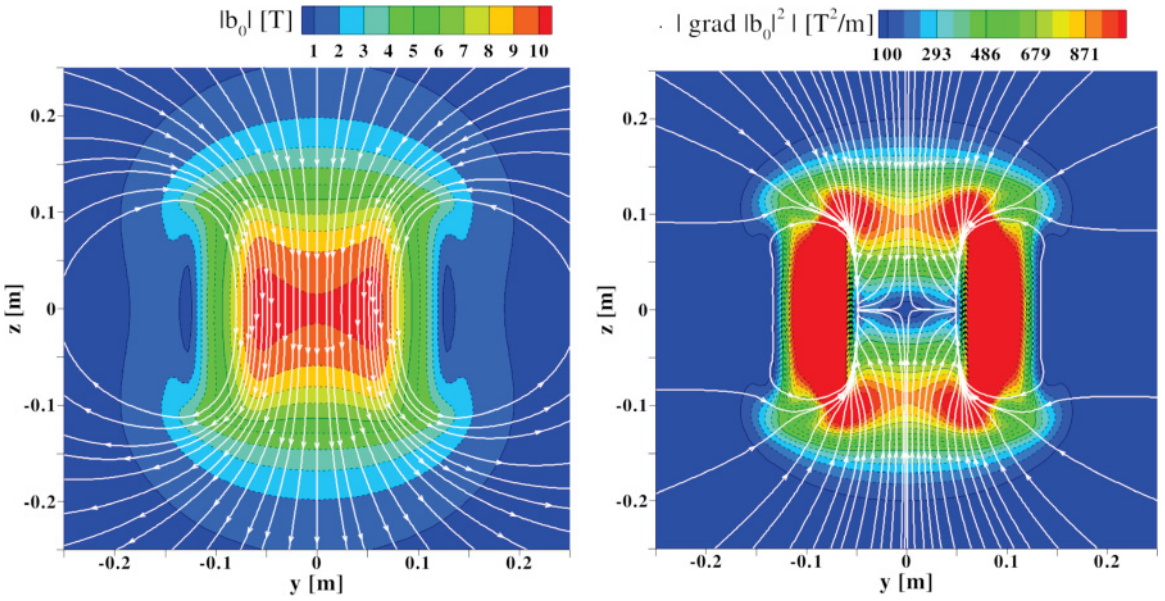

FIG. 2. (Color online) Calculated distributions of magnetic field (contours) and magnetic flux (lines) (left) and of the magnitude of the magnetic square gradients (right) in the central vertical plane (y-z) of the simulated experimental setup shown in Fig. 1 for the upper limit of working conditions, i.e., $|b_0|_{\max} = 10$ T.

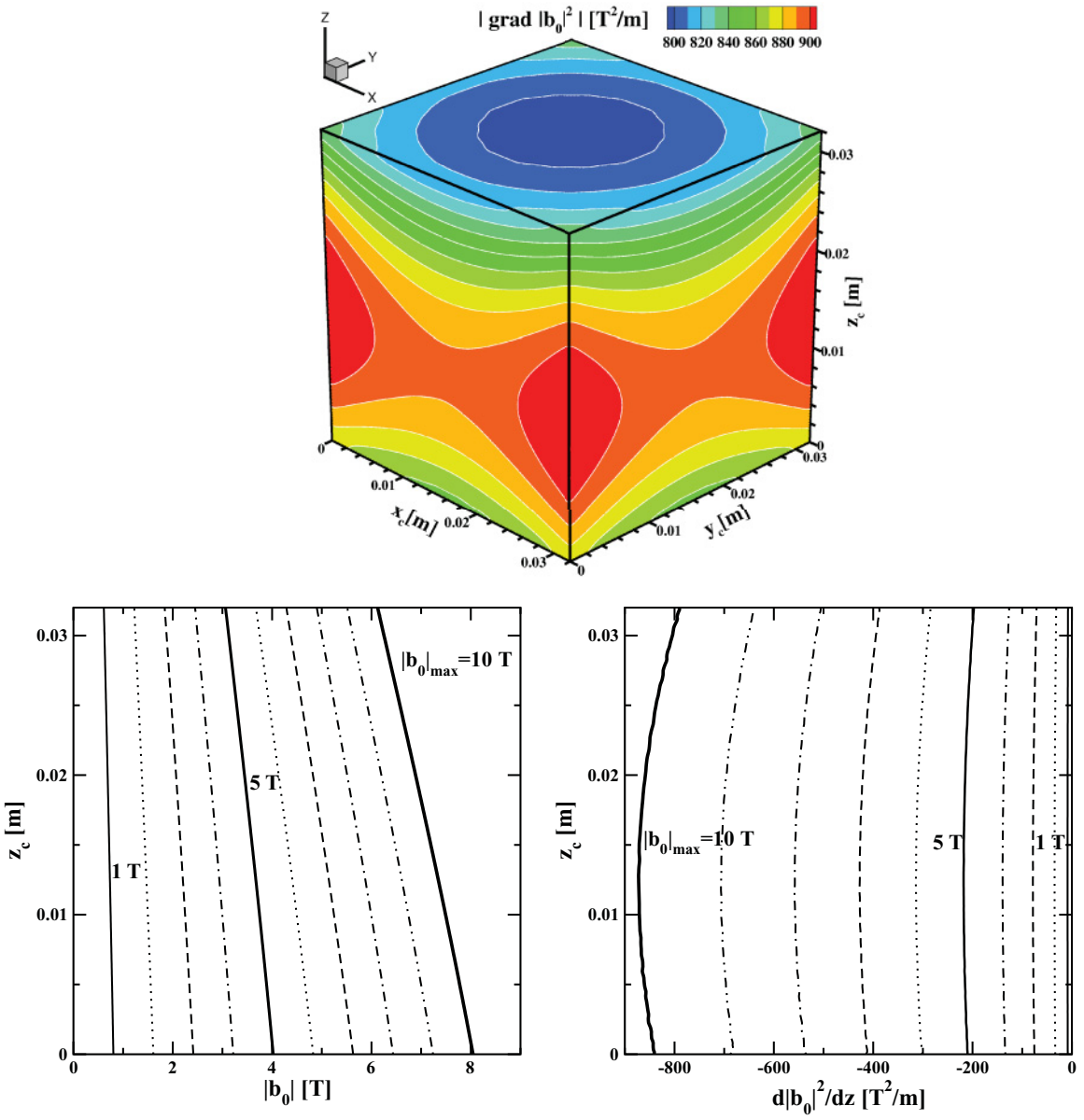

FIG. 3. (Color online) Top: Contours of the magnitude of the gradient of the square of the magnetic field (for $|b_0|_{\max} = 10$ T) within the cubical enclosure. Bottom: The vertical profiles of $|b_0|$ (left) and of $d|b_0|^2/dz$ (right) in the central vertical plane ($y_c = 0.016$ m, $x_c = 0.016$ m, $0 \leqslant z_c \leqslant 0.032$ m) for the entire range of imposed magnetic field, $0 \leqslant |b_0|_{\max} \leqslant 10$ T.

where additional forces are the thermal buoyancy ($\mathbf{f}^B$) and magnetization ($\mathbf{f}^M$), which can be written (by applying the Boussinesq approximation) as

$$\mathbf{f}^B = -\beta\,(\theta - \theta_0)\,\mathbf{g}, \tag{2}$$

$$\mathbf{f}^M = -\frac{1}{\rho}\left(1 + \frac{1}{\beta\theta_0}\right)\frac{\chi\beta\,(\theta - \theta_0)}{2\mu_0}\nabla|b_0|^2. \tag{3}$$

The magnetisation force is modeled by taking the magnetic susceptibility as temperature dependent [5,6,9,11–16]. Here, $\theta_0 = (\theta_h + \theta_c)/2$ is the reference temperature, ν is the kinematic viscosity, β is the thermal expansion coefficient, $\mathbf{g}$ (0,0, − 9.81) m/s^2 is the gravitational vector, and $|b_0|$ is the magnetic field strength. Note that there is an analogy between the gravitational and magnetization forces for a weakly nonlinear magnetic field distribution (for the vertical velocity component). But this analogy is incomplete due to weak spanwise components of the magnetization force. The temperature equation can be written as

$$\frac{\partial\theta}{\partial t} + (\mathbf{u}\cdot\nabla)\,\theta = \frac{\nu}{\mathrm{Pr}}\nabla^2\theta. \tag{4}$$

Together with the divergency-free conditions for velocity ($\nabla\cdot\mathbf{u} = 0$) and magnetic fields ($\nabla\cdot\mathbf{b} = 0$), this makes a fully closed system of transport equations. The stationary magnetic field distribution is calculated from Biot-Savart's law for a current-carrying coil of the superconducting magnet as

$$\mathbf{b} = \frac{\mu_0 I}{4\pi}\int\frac{d\mathbf{s}\times\mathbf{r}}{r^3}, \tag{5}$$

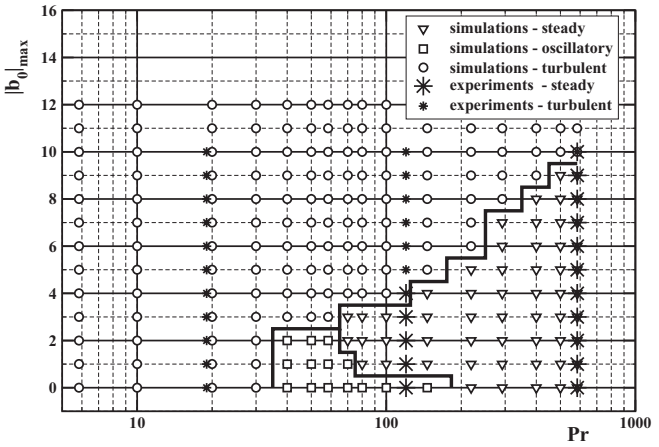

FIG. 4. Stability diagram (steady, oscillatory, and turbulent states) for a cubical enclosure, heated from below and cooled from above, with $\Delta\theta = \theta_h - \theta_c = 5\,^{\circ}\mathrm{C}$, over a range of Pr numbers ($5.84 \leqslant \mathrm{Pr} \leqslant 700$) and of the imposed magnetic field ($0 \leqslant |b_0|_{\max} \leqslant 12$ T).

where I is the strength of the electric current, r is the distance from a wire, and $d\mathbf{s}$ is the length of the differential element of the current-carrying wire [6]. Note that despite the constant value of the imposed magnetic field, the magnetization force is not constant since it depends on the local temperature. The analyzed phenomenon is fully determined by three characteristic nondimensional groups: the Prandtl number ($\mathrm{Pr} = \nu/a$, which is in the $5 \leqslant \mathrm{Pr} \leqslant 700$ range), the thermal Rayleigh number [$\mathrm{Ra_T} = g\beta\Delta\theta\mathrm{Pr}\,(\rho/\mu)^2\,D^3$, which is in the $1.15 \times 10^5 \leqslant \mathrm{Ra_T} \leqslant 8 \times 10^6$ range] and the magnetization number ($\gamma = \chi_0|b_0|^2_{\max}/\mu_0 g D$, which is in the $0 \leqslant \gamma \leqslant 58.5$ range). The nondimensional forms of the momentum and energy equations can now be written as

$$\frac{\partial \mathbf{u}^*}{\partial t} + (\mathbf{u}^* \cdot \boldsymbol{\nabla})\mathbf{u}^* = -\boldsymbol{\nabla} p^* + \mathrm{Pr}\nabla^2\mathbf{u}^* + \mathrm{Pr}\theta^*(\mathrm{Ra_T} + \mathrm{Ra_M}), \quad (6)$$

$$\frac{\partial \theta^*}{\partial t} + (\mathbf{u}^* \cdot \boldsymbol{\nabla})\theta^* = \nabla^2\theta^*, \quad (7)$$

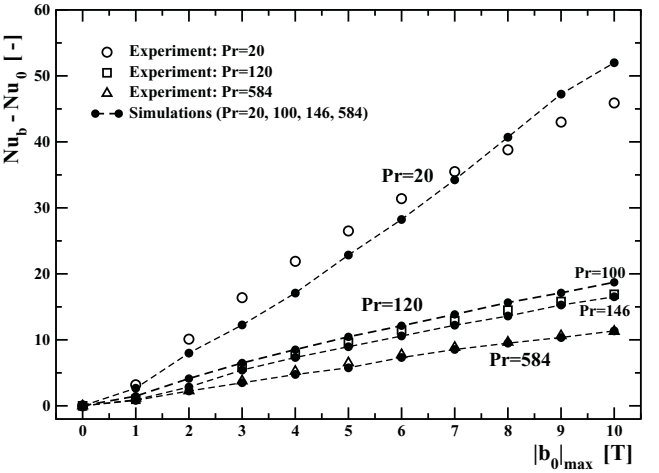

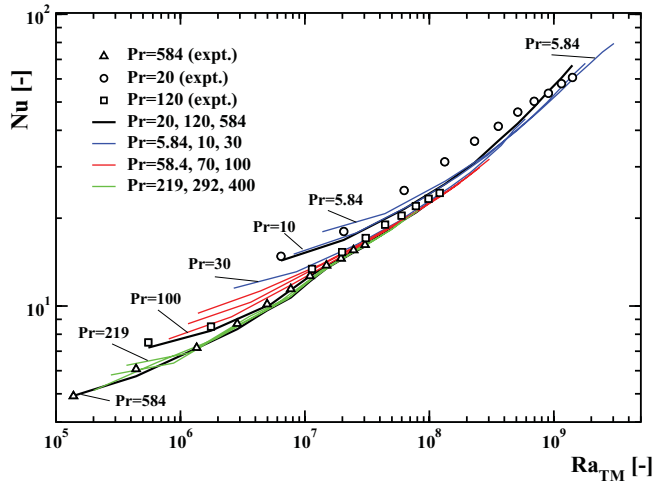

FIG. 6. (Color online) Top: Comparative assessment of measured and simulated integral heat transfer (Nu) for different values of Pr and of the imposed magnetic field. $\mathrm{Nu_0}$ is the Nusselt number for the neutral state, i.e., without imposed magnetic field. Bottom: The Nusselt number versus the thermal-gravitational-magnetic Rayleigh number ($\mathrm{Ra_{TM}} = \mathrm{Ra_T} + \mathrm{Ra_M}$) for the selected cases shown in Fig. 4.

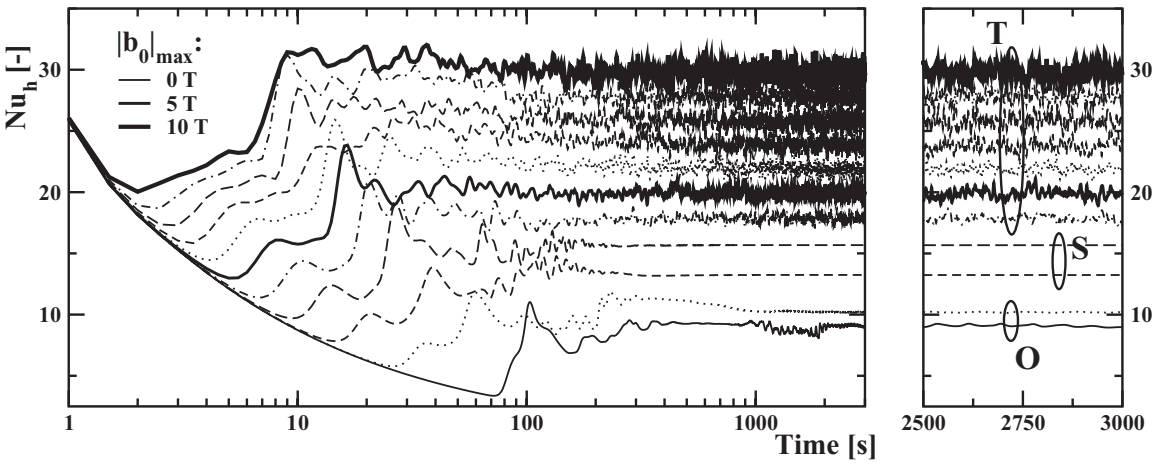

FIG. 5. Left: Time evolution of the averaged Nusselt number at the hot horizontal wall for $\mathrm{Pr} = 70$ and different strengths of the imposed magnetic field, $0 \leqslant |b_0|_{\max} \leqslant 10$ T. Right: Enlarged 2500–3000 s time interval. O, oscillatory; S, steady; T, turbulent.

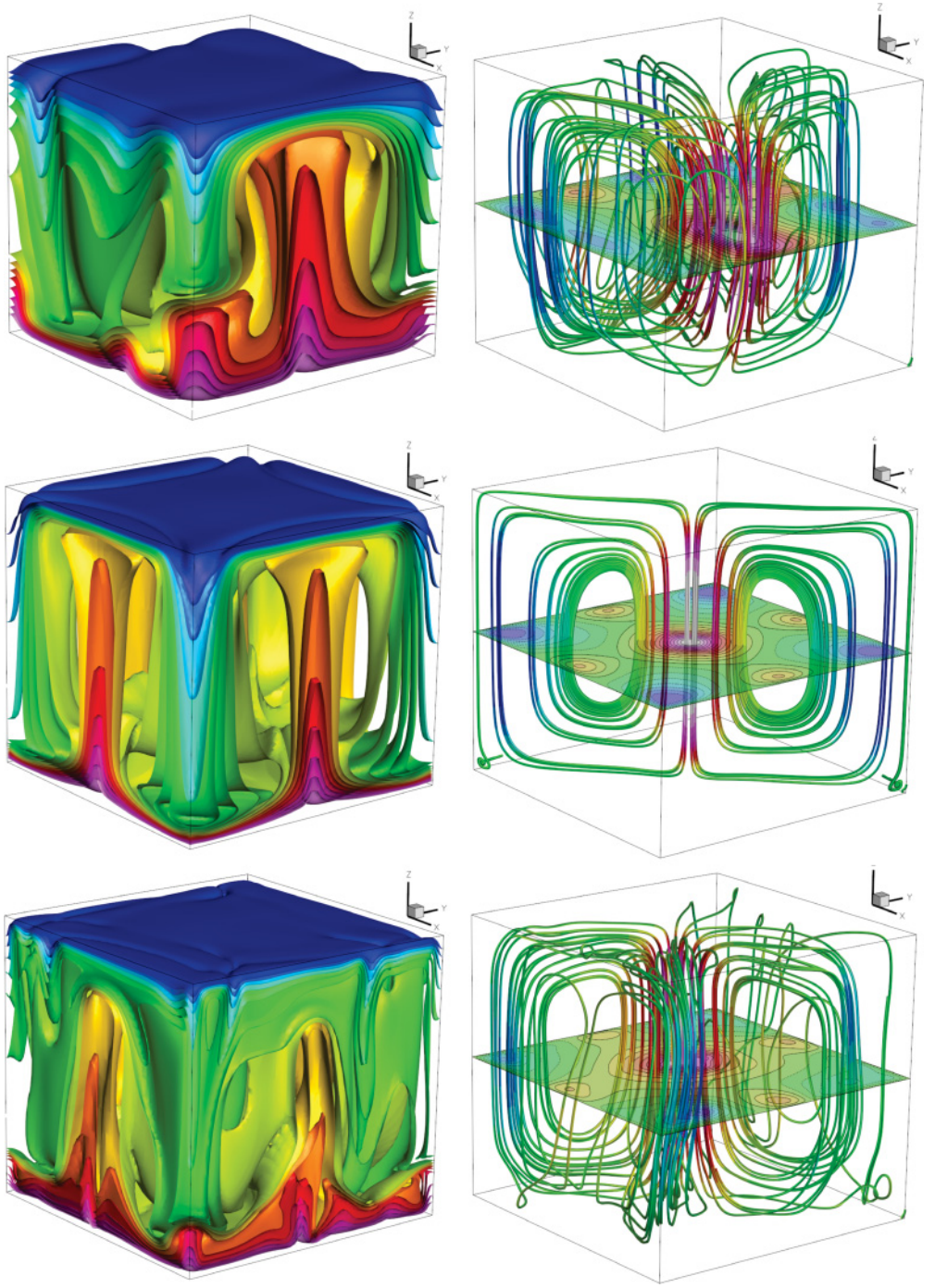

FIG. 7. (Color online) Thermal plumes (15 isosurfaces of temperature, $\theta_{\max} = 25\,^{\circ}\mathrm{C}$, $\theta_{\min} = 20\,^{\circ}\mathrm{C}$) (left) and stream traces (colored by vertical velocity, whose contours are also plotted in the central horizontal plane) (right) in a cubical enclosure heated from below and cooled from above with a constant temperature difference $\Delta\theta = 5\,^{\circ}\mathrm{C}$, $\mathrm{Pr} = 70$, and for different intensities of the imposed magnetic field, $|b_0|_{\max} = 0$ (top), 2 (middle), and 5 T (bottom).

where the magnetic Rayleigh number is defined as $\mathrm{Ra_M} = \gamma^*\beta\Delta\theta\mathrm{Pr}(\rho/\mu)^2D^3$, $\gamma^* = \gamma g[1 + 1/(\beta\theta_0)]/2$, and $\mathbf{u}^* = \mathbf{u}/u_0$, $u_0 = \nu/(\mathrm{Pr}D)$, $\theta^* = (\theta - \theta_0)/(\theta_h - \theta_c)$.

The system of equations (1)–(5) is discretized and iteratively solved by a three-dimensional finite-volume-based integrated Navier-Stokes–Maxwell numerical solver for general nonorthogonal geometries (for more numerical details see [17–25]). The simulations are performed on a numerical mesh containing 82^3–122^3 control volumes (CVs) that are nonuniformly distributed in the proximity of all walls in order to properly capture the development of hydrodynamic and thermal boundary layers (10–20 CVs are located within boundary layers).

The contours and vertical profiles of the intensity of the magnetic field and its gradients within the cubical enclosure [obtained by solving Eq. (5)] are shown in Fig. 3. The

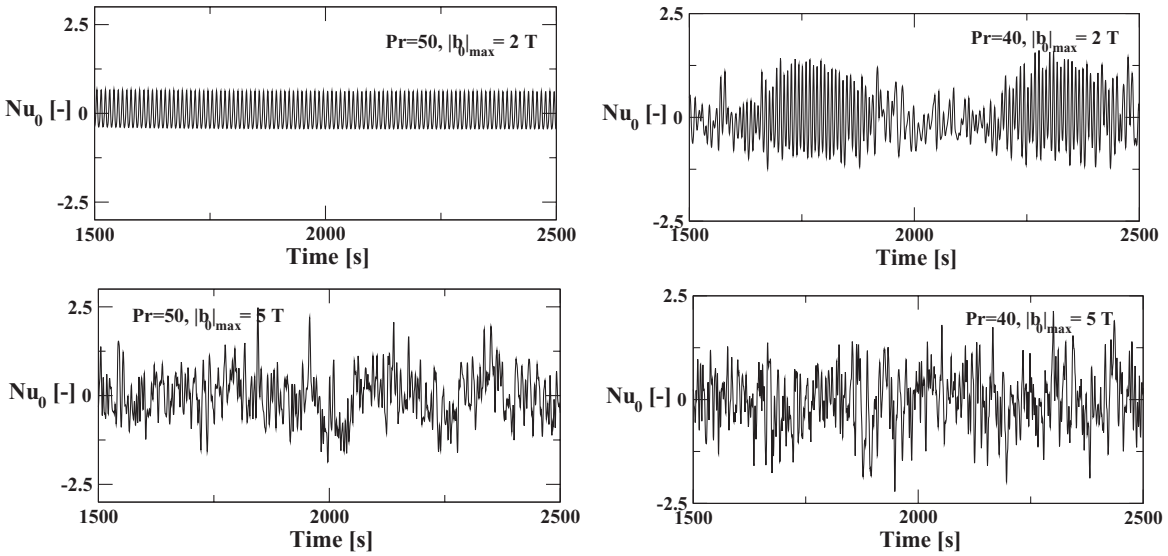

FIG. 8. The oscillatory (periodic) (top) and turbulent (bottom) regimes: time evolutions of the integral heat transfer $\mathrm{Nu}_0 = \mathrm{Nu}_h + \mathrm{Nu}_c$ for $\mathrm{Pr} = 50$ (left) and 40 (right), for $|b_0|_{\max} = 2$ (top) and 5 T (bottom), respectively.

vertical magnetic field profiles have approximately linear distributions; Fig. 3, bottom left. The results of all simulations and experiments for different Pr and applied $|b_0|_{\max}$ are shown in Fig. 4. All results are obtained for a fixed temperature difference of $\Delta\theta = 5\,^{\circ}\mathrm{C}$. This is done to minimize the variation of the fluid physical properties and to satisfy the Boussinesq approximation. Three distinct regimes can be identified: steady, oscillatory (periodic), and turbulent states. The experiments ($*$) and simulations ($\square$) show a very good agreement in identifying the steady and turbulent regimes. In addition to correct predictions of the prevailing oscillatory (for lower Pr) and stable (for higher Pr) regimes, a transition location from an initially stable to an oscillatory state is also properly captured ($\mathrm{Pr} = 120$ and $|b_0|_{\max} = 4$ T). Particularly interesting are the oscillatory states that are numerically identified for intermediate values of Pr ($40 \leqslant \mathrm{Pr} \leqslant 70$) and low magnetic field ($|b_0|_{\max} \leqslant 2$ T). Note that nonmonotonic behavior is present in the $70 \leqslant \mathrm{Pr} \leqslant 200$ range. Here, the periodic states for neutral situation are first stabilized by stronger magnetic fields. Then, with further increase of the imposed magnetic field gradients, turbulent states are generated; see Fig. 5. Next, we performed a comparative assessment of the measured and simulated long-term-averaged heat transfer enhancement ($\mathrm{Nu}_b - \mathrm{Nu}_0$) for different values of Pr and magnetic fields; Fig. 6, top. It can be seen that the agreement is excellent for high Pr numbers ($\mathrm{Pr} = 120$ and 584) over the entire range of the applied magnetic fields (simulations are shown for $\mathrm{Pr} = 100$, 146, and 584). For $\mathrm{Pr} = 20$, the qualitative agreement is also good, with some deviations for stronger magnetic fields, which most probably can be attributed to some uncontrolled heat losses in experiments (the heat transfer is higher for lower Pr and accordingly heat losses will increase). Note that compared to its neutral state, a significant heat transfer is obtained for the magnetically active cases. The integral heat transfer enhancement $[(\mathrm{Nu}_b/\mathrm{Nu}_0) - 1]$ is in the range from 15% (for $|b_0|_{\max} = 1$ T) to 330% (for $|b_0|_{\max} = 10$ T).

A summary of selected simulations and measurements is given in Fig. 6, bottom, where the thermal-gravitational-magnetic Rayleigh number ($\mathrm{Ra}_{\mathrm{TM}} = \mathrm{Ra}_{\mathrm{T}} + \mathrm{Ra}_{\mathrm{M}}$) is used as the scaling parameter. Three distinct regimes can be identified. The first is a transient regime where the thermogravitational and thermomagnetic mechanisms are both important, $\mathrm{Ra}_{\mathrm{TM}} \leqslant 3 \times 10^7$. Then, a thermomagnetic mechanism starts to take over in the $3 \times 10^7 < \mathrm{Ra}_{\mathrm{TM}} \leqslant 3 \times 10^8$ range. A new change in the Nusselt number slope is observed for $\mathrm{Ra}_{\mathrm{TM}} > 3 \times 10^8$, indicating additional wall-heat transfer increase.

To portray the three-dimensional morphology of the temperature and velocity field, we plotted snapshots of the thermal plumes and stream traces for $\mathrm{Pr} = 70$ and for different magnetic fields; Fig. 7. We selected the $\mathrm{Pr} = 70$ case since it includes the double transition already discussed, i.e., an initially oscillatory (periodic) motion for the neutral case is first stabilized by imposing a weak magnetic field ($2 \leqslant |b_0|_{\max} \leqslant 3$ T), and then turbulent states are generated with stronger magnetic fields ($|b_0|_{\max} \geqslant 4$ T); see Figs. 4 and 5.

Changes in the structure of thermal plumes during these transitions are clearly visible; Fig. 7. For neutral case, the spatial orientation of the thermal plumes does not indicate any alignment with the main enclosure diagonals; Fig. 7, top. This is the result of an intensive horizontal meandering of the thermal plumes. Perfect symmetrical distributions of thermal plumes are obtained for stable conditions; Fig. 7, middle. Now, four vertical updrafts originating from the centers of intersections between the bottom wall and sidewalls, while the vertical downdrafts occupy the corner regions. A prominent central vertical updraft can be observed from imprints of the vertical velocity contours in the central horizontal plane; Fig. 7, middle right. Stronger magnetic fields ($|b_0|_{\max} = 5$ T) generate multiple vertical ejections from the horizontal boundary layers along the sidewalls, as seen in Fig. 7, bottom left. Imprints of these vertical ejections are not visible in the central horizontal plane (Fig. 7, bottom right), indicating their weak penetrative

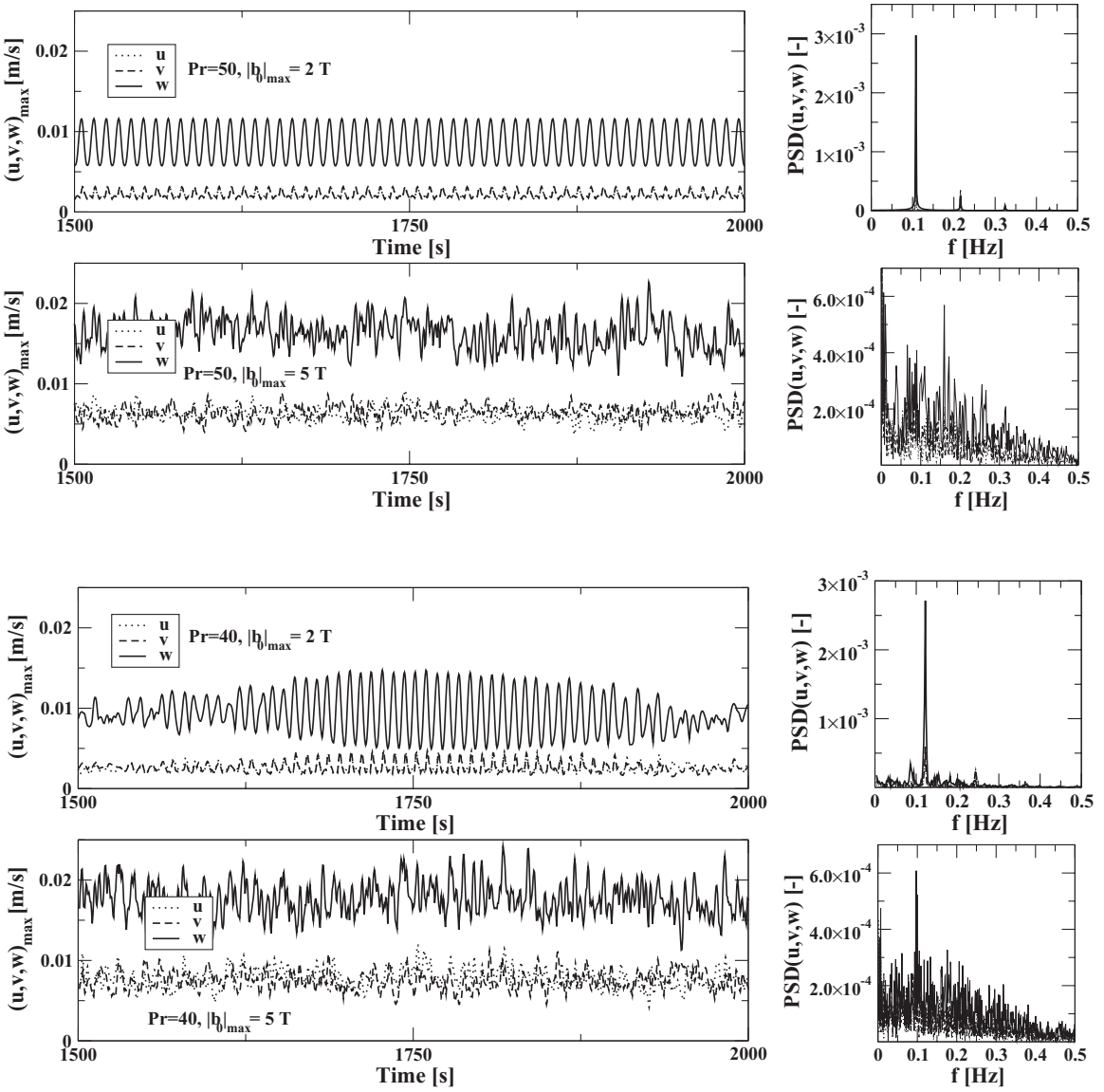

FIG. 9. Time evolutions of the maximum velocity components (left) and their power spectrum densities (right) for Pr = 40 and 50, $|b_0|_{\max} = 2$ and 5 T. Oscillatory states are observed for $|b_0|_{\max} = 2$ T, Pr = 40 and 50, and turbulent states for $|b_0|_{\max} = 5$ T, Pr = 40 and 50.

capabilities. The five-updraft and four-downdraft morphology of thermal plumes is still kept, but horizontal meandering of plumes leads to breaking of the diagonal symmetry in the spatial orientation of the thermal plumes, which is not visible anymore at $|b_0|_{\max} = 6$ T.

Time series of $\mathrm{Nu}_0 = \mathrm{Nu}_h + \mathrm{Nu}_c$ for Pr = 40 and 50 and $|b_0|_{\max} = 2$ and 5 T are depicted in Fig. 8. By increasing the imposed magnetic field, transients from the oscillatory states with a single dominant frequency to fully developed turbulent states are generated. Changes in morphology of the thermal plumes are also visible in time series of the maximum velocity components; Fig. 9, left. A strong correlation between Nu_0 (shown in Fig. 8) and the vertical velocity (w) is clearly visible, confirming that the vertical ejection of thermal plumes is the main mechanism for the heat transfer. The time series of the horizontal velocity components (u and v) are identical for steady and oscillatory states. Small changes between the horizontal velocity components start to appear for $|b_0|_{\max} = 2$ T, and are clearly visible for $|b_0|_{\max} = 5$ T. These differences in the time series of the maxima of the horizontal velocity components indicate the presence of three-dimensional instabilities that originate from symmetry breaking of the centrally dominant thermal plume, similar to that shown in Fig. 7. This transition from the oscillatory to the turbulent state is also depicted in power spectrum density distributions; Fig. 9, right. Here, a spectrum with a few discrete frequencies (for Pr = 40 and Pr = 50, with $|b_0|_{\max} = 2$ T) is replaced with a more continuous spectrum with a wide range of frequencies (for $|b_0|_{\max} = 5$ T), confirming turbulent behavior.

In conclusion, we have presented a stability map of fthe low and heat transfer regimes for thermomagnetic convection of a paramagnetic fluid subjected to strong magnetic field gradients over an extensive range of working

parameters. Good agreement between experiments and three-dimensional time-dependent numerical simulations in predicting integral heat transfer has been obtained. Nonmonotonic behavior of the integral heat transfer coefficient with an increase of the imposed magnetic field gradients (initially stabilizing and then destabilizing effects) has been observed in the ranges $70 \leqslant \mathrm{Pr} \leqslant 146$ and $1 \leqslant |b_0|_{\max} \leqslant 4$ T.

[1] G. Ahlers, G. Siegfied, and D. Lohse, Rev. Mod. Phys. **81**, 503 (2009).
[2] R. W. Series and D. T. J. Hurle, J. Cryst. Growth **113**, 305 (1991).
[3] N. I. Wakayama, Cryst. Growth Design **3**, 17 (2003).
[4] D. Braithwaite, E. Beaugnon, and R. Tournier, Nature (London) **354**, 134 (1991).
[5] J. Qi, N. I. Wakayama, and A. Yabe, Int. J. Heat Mass Transfer **44**, 3043 (2001).
[6] T. Tagawa, R. Shigemitsu, and H. Ozoe, Int. J. Heat Mass Transfer **45**, 267 (2002).
[7] S. Maki, M. Ataka, T. Tagawa, H. Ozoe, and W. Mori, AIChE J. **51**, 1096 (2005).
[8] T. Bednarz, E. Fornalik, T. Tagawa, H. Ozoe, and J. S. Szmyd, Int. J. Therm. Sci. **44**, 933 (2005).
[9] S. Maki, M. Ataka, T. Tagawa, and H. Ozoe, Phys. Fluids **19**, 087104 (2007).
[10] M. Akamatsu, M. Higano, and H. Ozoe, Numer. Heat Transfer, Part A **51**, 159 (2007).
[11] T. Bednarz, C. Lei, J. C. Patterson, and H. Ozoe, Int. J. Therm. Sci. **48**, 26 (2009).
[12] W. Wrobel, E. Fornalik-Wajs, and J. S. Szmyd, Int. J. Heat Fluid Flow **31**, 1019 (2010).
[13] J. Huang, B. F. Edwards, and D. D. Gray, Phys. Fluids **9**, 1819 (1997).
[14] J. Huang, D. D. Gray, and B. F. Edwards, Phys. Rev. E **57**, 5564 (1998).
[15] J. Huang, B. F. Edwards, and D. D. Gray, Phys. Rev. E **57**, R29 (1998).
[16] R. Ganguly, S. Sen, and I. K. Puri, Phys. Fluids **16**, 2228 (2004).
[17] S. Kenjereš and K. Hanjalić, Int. J. Heat Fluid Flow **20**, 329 (1999).
[18] S. Kenjereš and K. Hanjalić, Phys. Rev. E **62**, 7987 (2000).
[19] S. Kenjereš and K. Hanjalić, Phys. Rev. E **66**, 036307 (2002).
[20] S. Kenjereš and K. Hanjalić, Int. J. Heat Fluid Flow **27**, 800 (2006).
[21] S. Kenjereš and K. Hanjalić, Phys. Rev. Lett. **98**, 104501 (2007).
[22] S. Kenjereš and K. Hanjalić, New J. Phys. **9**, 1 (2007).
[23] S. Kenjereš, Phys. Rev. E **78**, 066309 (2008).
[24] S. Kenjereš, Int. J. Heat Fluid Flow **29**, 752 (2008).
[25] S. Kenjereš, Phys. Fluids **23**, 015103 (2011).